ADVANCED FUNCTIONAL MATERIALS
www.afm-journal.de

Circularly Polarized Mechanoluminescence for Force-Insensitive Optical Information Decryption

Xiaolin Nie, Chunfeng Wang, Xinye Lu, Gaofeng Lai, Zugang Li, Dengfeng Peng, Weidong Chen, Deliang Zhu,* and Caofeng Pan**

Stimuli-responsive materials that exhibit circularly polarized luminescence (CPL) have attracted significant attention for applications in chiroptical sensing and information security. However, the development of CPL platforms remains limited owing to the challenges in chirality control, reliance on photoexcitation, and complexity of the decoding mechanisms. In this paper, a force-insensitive chiroptical platform is presented, constructed by integrating a mechanoluminescent phosphor layer with a photonic crystal layer. The phosphor layer enables both photoluminescence (PL) and mechanoluminescence (ML) emissions, whereas the photonic crystal layer enables tunable photonic bandgaps, achieved by adjusting the cellulose nanocrystal-to-glucose ratio. This structural design enables modulated CPL with high dissymmetry factors (g_{lum}), reaching −0.512 and −0.573 for g_{PL} and g_{ML}, respectively. Further, the system shows distinct solvent-responsive circularly polarized mechanoluminescence (CPML) behavior. Moreover, its force-insensitive response offers a robust and light-free strategy for information decryption, significantly enhancing security while simplifying operation. These findings highlight the potential of the CPML platform for next-generation chiroptical sensing and secure information technologies.

1. Introduction

Chirality is a pervasive phenomenon in nature, manifesting across a wide range of length scales from molecular to macroscopic structures. As a classical chiroptical phenomenon, circularly polarized luminescence (CPL) refers to the differential emission of left- (L-CPL) and right-handed (R-CPL) circularly polarized light from chiral materials. Dissymmetry factor (g_{lum}) is the key parameter used to quantify CPL, defined as $g_{lum} = 2(I_L - I_R)/(I_L + I_R)$, where I_L and I_R denote the intensities of left- and right-handed CPL, respectively. Owing to the unique chiral-recognition capabilities, CPL materials are promising for a wide range of advanced technologies, including optoelectronic devices, asymmetric synthesis, information security, and stereoscopic displays.[1–10] In recent years, the scope of research into CPL materials has expanded beyond the chiral lanthanide complexes to encompass a broad range of materials, including chiral metal hybrids,[11–13] perovskite materials,[14–17] and small organic molecules.[18–21] However, conventional CPL materials are limited by undesirable, uncontrollable, and stimulus nonresponsive g_{lum} values, which constrain their practical applications and hinder their functionality.

Photonic crystals (PCs) are periodic dielectric structures with photonic bandgaps (PBGs) that enable the selective manipulation of photons having specific wavelengths. Thus, they serve as ideal platforms for enhancing the chiroptical-emission properties. Cellulose nanocrystals (CNCs) are a sustainable, easily processable, and structurally tunable class of natural PC materials, which can form left-handed cholesteric liquid-crystalline structures through controllable solvent-evaporation-induced self-assembly, making them particularly attractive for chiral photonic applications.[22–24] A distinctive optical feature of this structure is its selective transmission of CPL. When guest emitters or composite emissive layers generate light at specific wavelengths, the CNCs can modulate the emission into CPL. The helical pitch (P) of CNCs can be efficiently and precisely modulated by external stimuli, such as electrolytes, ultrasound, thermal fields, or electromagnetic fields, enabling accurate control over chiroptical signals. The quantitative relationship between the PBG and P can be described by the Bragg equation: $\lambda_{PBG} = n_{ave} \times P \times \sin\theta$, where n_{ave} represents

X. Nie, C. Wang, X. Lu, G. Lai, Z. Li, D. Zhu
Guangdong Research Center for Interfacial Engineering of Functional Materials
Guangdong Provincial Key Laboratory of New Energy Materials Service Safety
College of Materials Science and Engineering
Shenzhen University
Shenzhen, Guangdong 518060, China
E-mail: cfwang@szu.edu.cn; dlzhu@szu.edu.cn

D. Peng
Key Laboratory of Optoelectronic Devices and Systems of Ministry of Education and Guangdong Province
College of Physics and Optoelectronic Engineering
Shenzhen University
Shenzhen, Guangdong 518060, China

W. Chen, C. Pan
Institute of Atomic Manufacturing
International Research Institute for Multidisciplinary Science
Beihang University
Beijing 100191, China
E-mail: 11513@buaa.edu.cn

The ORCID identification number(s) for the author(s) of this article can be found under https://doi.org/10.1002/adfm.202526708

DOI: 10.1002/adfm.202526708

the average refractive index of the material, and θ is the angle between the incident light and the chiral layer.[5,25,26] When the emission wavelength closely matches the PBG, the circularly polarized component with the same handedness as the helical structure is suppressed, whereas the opposite-handed component is selectively transmitted. In recent years, the PBG effect serves as a determining factor for achieving high g_{lum} values. For example, Yuan et al. demonstrated that the CPL signals, particularly the g_{lum} value, could be effectively controlled and even reversed through precise modulation of the PBG.[27] Yu et al. reported a controllable and macroscopic production of printable CPL-active photonic paints, achieving a maximum g_{lum} value of 1.6 by PBG tuning.[28] In our previous work, a series of biomimetic hybrid photonic films were fabricated. By leveraging hydrogen bonding and the PBG effect, a high g_{lum} value of -0.650 for circularly polarized phosphorescence was achieved.[29] Additionally, we have previously demonstrated that CNCs can respond to moisture as an external stimulus.[29,30] Consequently, moisture-responsive CPL materials with PBG tuning can be developed, presenting promising opportunities for applications in smart sensing, novel information encryption, and anticounterfeiting technologies.

However, owing to their intrinsic material limitations, current CPL systems generally rely on specific excitation wavelengths, such as high-energy ultraviolet or near-ultraviolet light, preventing their use under light-free or autonomous conditions. In contrast, mechanoluminescence (ML) materials, which dynamically emit light in response to mechanical stimuli, such as compression, stretching, friction, vibration, or ultrasound, have distinct advantages, including ease of fabrication, operation without external excitation sources, and broad applicability across diverse environments.[31–43] Their unique mechano-to-optical energy-conversion mechanism and force-light coupling effect have enabled innovative applications in areas such as advanced light sources, wearable electronics, energy harvesting, anticounterfeiting encryption, intelligent sensing, biomedical diagnostics, and structural health monitoring.[44–53] These features present new opportunities for developing CPL systems. In our previous work, we synthesized an enantiomeric pair of 0D hybrid manganese-bromide enantiomers, (*R*/*S*)-1, that produced circularly polarized mechanoluminescence (CPML) emission.[54–56] However, the dissymmetry of CPML is not clearly understood, and the crystalline materials are constrained by their poor reusability and limited applications.

Herein, we address the inherent reliance of conventional CPL materials on high-energy excitation sources by drawing inspiration from an ML system. Briefly, we developed an innovative and reusable CPML platform that integrates ML phosphors and PCs. The phosphor layer comprises CaZnOS:Mn powders embedded in a polydimethylsiloxane (PDMS) matrix, and the PC layer consists of CNCs and glucose. In this case, glucose acts as a modulator for PBG tuning. Benefiting from the optimized matching between the ML emission band and PBG, the platform achieves asymmetry factors of −0.512 and −0.573 for g_{PL} and g_{ML}, respectively. Unlike conventional ML materials whose responses are sensitive to the magnitude of the force, this platform achieves a force-insensitive g_{ML} values. With its high asymmetry and stimulus-responsive characteristics, this CPML platform offers strong potential for applications in information security, intelligent sensing, and advanced optical technologies.

2. Results and Discussion

Scheme 1 illustrates the design of a CPML platform that eliminates the need for high-energy excitation sources, enables force-insensitive optical information decryption, provides a force-insensitive g_{lum} value, and achieves an optimized asymmetric chiral emission through PBG modulation. The platform comprises two integrated components, including a phosphor layer and a PC layer. The phosphor layer, with a thickness of 3.57 ± 0.05 mm, is composed of a PDMS elastomer embedded with CaZnOS:Mn phosphors that emit light upon mechanical excitation. On top of this, a PC layer was fabricated via in situ self-assembly, with a tunable thickness of 95.67 ± 11.32 to 226 ± 19.03 µm governed by the glucose concentration, and serves as a chiral photonic structure that modulates the ML via the PBG effect to generate CPML. We employed CNCs, obtained via acid hydrolysis of commercial

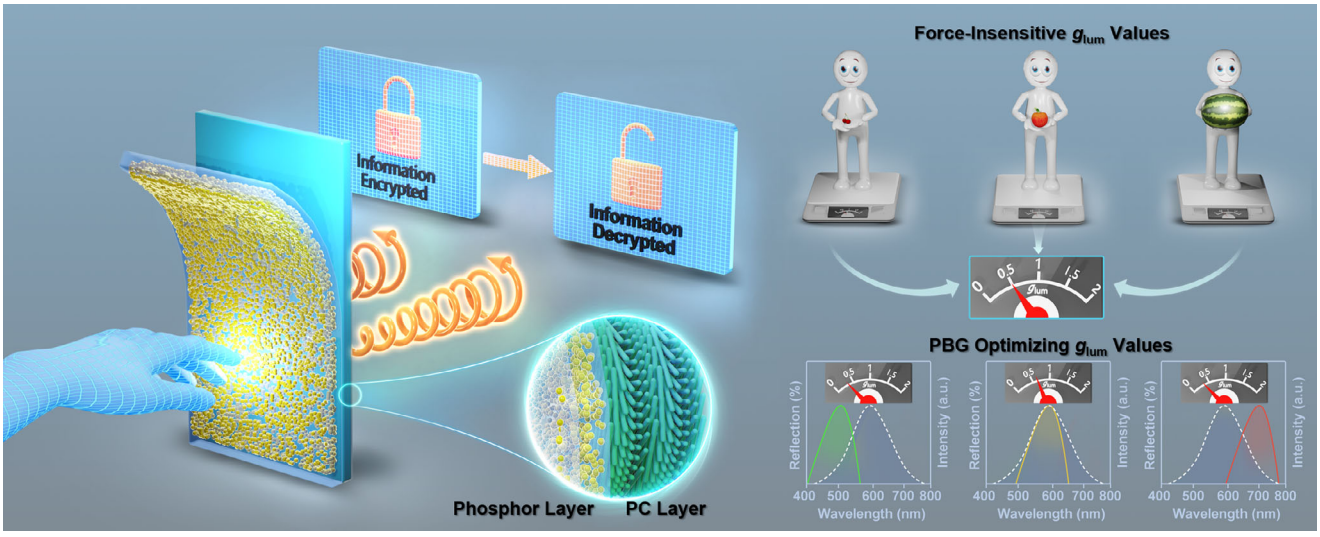

Scheme 1. Design of a CPML platform featuring information decryption, force-insensitive g_{lum} value, and PBG-optimized chiral emission.

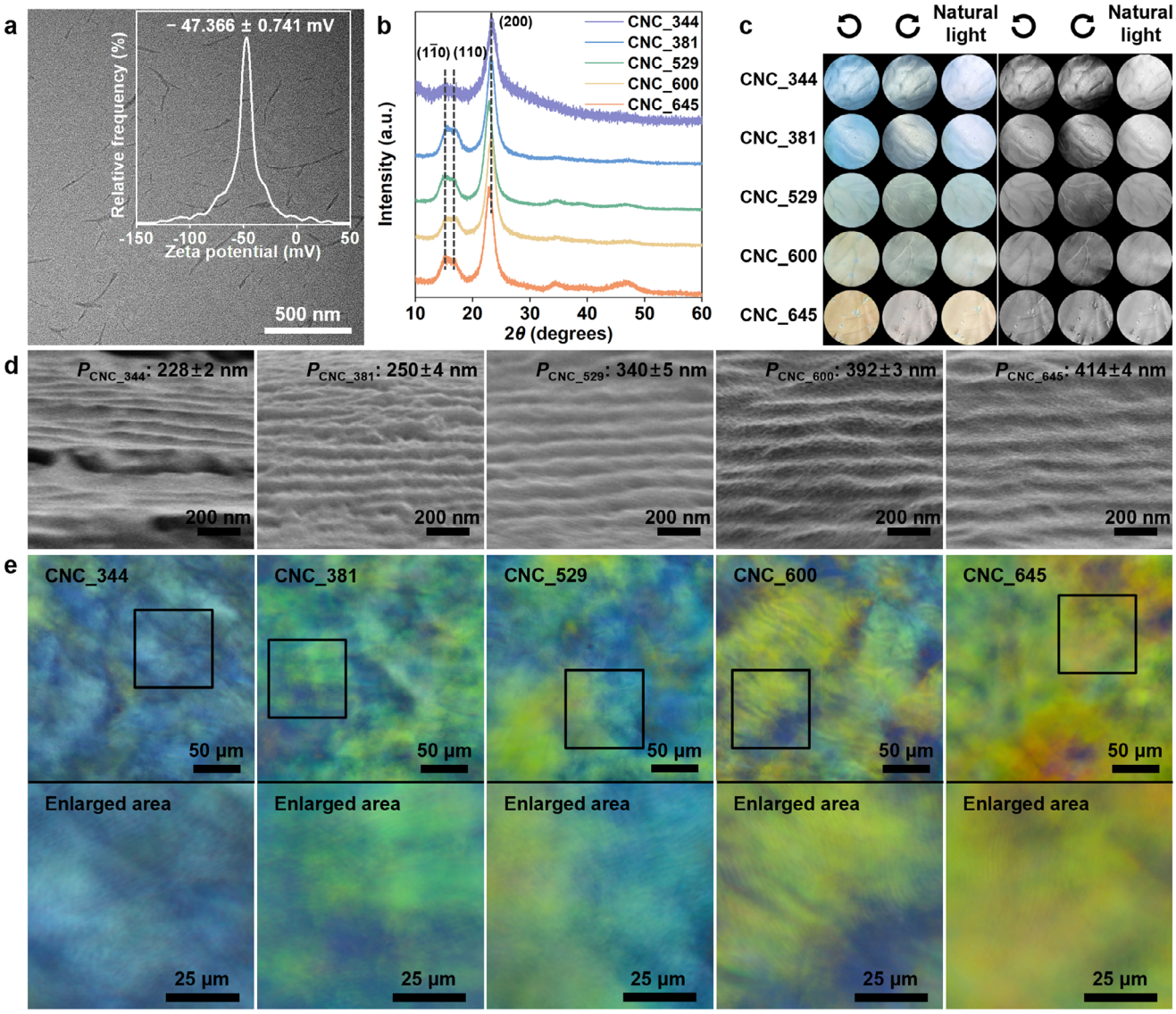

Figure 1. Characterization of CNCs and CNC PC layers: a) TEM image of CNCs. Inset: ζ-potential of the CNC aqueous solution. b) X-ray diffractometry patterns, c) photographs and grayscale images, d) cross-sectional scanning electron microscopy images, and e) polarized optical microscopy images of PC layers with various PBGs.

powder with rigid cellulose I structure (Figure S1, Supporting Information), as the component for the PC layer. Transmission electron microscopy (TEM) images reveal that the CNCs have a well-dispersed rod-like morphology, attributed to the presence of negatively charged sulfate groups (ζ-potential: −47.366 mV) (**Figure** 1a inset). The CNC nanorods had an average length of 189 ± 30 nm (Figure S2a, Supporting Information) and a width of 19 ± 3 nm (Figure S2b, Supporting Information).

Glucose was used to modulate the *P* value of the PC layer and optimize the chiroptical asymmetry of the CPML platform, thereby fine-tuning the PBG and enhancing the circularly polarized emission. PC layers with PBGs of 344, 381, 529, 600, and 645 nm were self-assembled on the surface of the phosphor layer by adjusting the ratio of the CNCs to glucose. The XRD patterns (Figure 1b) exhibit three distinct diffraction peaks at $\approx 2\theta = 14.7°$, 16.6°, and 22.6°, corresponding to the (11_0), (110), and (200) planes of cellulose I, respectively, indicating that the PC layer was integrated without disrupting the native structure. However, the incorporation of glucose led to a noticeable shift in the structural color, from bright blue to orange (Figure 1c), indicative of glucose-induced PBG modulation, in accordance with Bragg's equation. Notably, the PC layers display more pronounced structural colors when viewed through a left-handed circularly polarized (left-CP) filter than through a right-handed circularly polarized (right-CP) filter. Grayscale analysis of the PC layers (Figure S3, Supporting Information) further corroborated this observation, with higher grayscale values recorded under the left-CP filter, confirming the left-handed chiral nematic structure. Cross-sectional scanning electron microscopy (SEM) images (Figure 1d) reveal well-defined and periodically ordered

layers, having P values increasing from 228 ± 2 to 414 ± 4 nm (Figure S4, Supporting Information) with the increase in glucose content, indicating a redshifted PBG. Concurrently, polarized optical microscopy (POM) observations revealed distinct birefringence and fingerprint textures (Figure 1e), further verifying the chiral nematic structure of the PC layers.

We employed a phosphor layer composed of CaZnOS:Mn powder embedded in a PDMS matrix as the excitation source to address the strong reliance of common CPL systems on excitation sources. CaZnOS was selected as the host material owing to its well-documented ML performance when doped with Mn or lanthanide ions. In this study, CaZnOS:Mn phosphors were synthesized using a conventional high-temperature solid-state method and subsequently characterized. As shown in **Figure 2**a, all the XRD diffraction peaks can be assigned to the hexagonal phase of CaZnOS (JCPDS No. 01-076-3819), confirming the synthesis of the desired crystalline phase. From the X-ray photoelectron spectroscopy (XPS) in Figure 2b, distinct signals corresponding to Ca, Zn, O, and S were obtained. Despite the inherently low sensitivity of XPS for Mn, the high-resolution spectrum reveals a clear Mn signal, containing a characteristic peak at 641.9 eV that can be attributed to the Mn^{2+} 2p orbital. Figure S5 (Supporting Information) shows the irregular morphology and size distribution of the phosphor powders, and a high-resolution TEM image of a selected region near the sharp epitaxial edge (Figure 2d) showed clear lattice fringes corresponding to CaZnOS (Figure 2e). Specifically, (010) lattice planes with an interplanar spacing of 3.726 Å are evident, indicating a well-crystallized CaZnOS phase. Accordingly, this observation is well-supported by the corresponding selected area electron diffraction (SAED) pattern (Figure 2f). From the high-resolution lattice elemental mapping images in Figure 2g, in addition to Ca, Zn, O, and S, uniformly dispersed Mn can be seen, confirming the incorporation of the Mn dopant, as also shown by XPS.

As shown in Figure 2h, the ML intensity increases with increasing Mn content, reaching a maximum at 2% doping. Beyond this concentration, the intensity decreased owing to quenching effects. Therefore, CaZnOS doped with 2% Mn was selected for phosphor-layer construction. Figure 2i shows the ML spectra recorded under applied forces ranging from 1 to 4 N, the emission intensity increases progressively with the applied force. The powders produced a bright orange light that is visible to the naked eye under both white light and in the dark when stimulated by grinding with a mortar and pestle (Figure 2i, inset). The corresponding integrated ML intensity as a function of force is plotted in Figure 2j, showing a linear relationship. Thus, CaZnOS doped with 2% Mn exhibits strong ML emission and high force sensitivity, making it a reliable basis for the development of CPML platforms.

Inspired by the unique characteristics of ML systems, we aimed to construct a CPML platform with the potential for advanced optical applications. In addition to the ML performance, the employed phosphor (CaZnOS:Mn) also exhibits photoluminescent behavior, enabling our CPML system to generate CPL under optical excitation. Under optimal excitation at 336 nm, the CaZnOS:Mn phosphors exhibit a prominent broad emission band, ranging from 500 to 800 nm (Figure S6a, Supporting Information) and centered at 591 nm. This emission is attributed to the characteristic transition of Mn^{2+} ions from the excited $^4T_1$ (^4G) to $^6A_1$ (^6S). Theoretically, the optimal alignment of the emission wavelength with the PBG results in a significant enhancement of the g_{PL} value (**Figure 3**a). To validate this strategy, the CPL and emission signal, including CPL, g_{PL}, and DC (emission signal was recorded by DC voltage) spectra, were acquired using a spectrophotometer. As shown in Figure 3b, all materials exhibit distinct R-CPL properties with varying CPL strengths. However, their DC spectra (Figure S7, Supporting Information) were identical, indicating that the observed differences in the CPL signals originate from variations in the chiroptical properties of the PC layer rather than luminescence from the CaZnOS:Mn phosphor layer. Next, the dissymmetry of the CPL was evaluated using g_{PL}, defined as $g_{PL} = 2(I_L - I_R)/(I_L + I_R)$. Theoretical g_{PL} values of −2 and +2 correspond to purely R- and L-CPL, whereas a value of 0 indicates no CPL. As shown in Figure 3c,d and Table S1 (Supporting Information), the measured g_{PL} values are −0.095, −0.180, −0.405, −0.512, and −0.355. As the PBG redshifts, the PL_591||CNC_600 sample exhibited the strongest CPL emission at a PBG of 600 nm, achieving the highest g_{PL} value.

The variation in the CPL intensity and optimization of the g_{PL} values are attributed to the tunable PBGs of the PC layers. These PC layers function as chirally selective optical filters, transforming their emissions into CPL through their helical chiral architecture. Specifically, the left-handed chiral domains suppress the transmission of L-CPL, thereby favoring R-CPL emission, as evidenced by the negative CPL signals observed (Figure 3b). As shown in Figure 3e, tuning the co-assembly ratio of the CNCs and glucose results in PC layers with distinct PBG positions at 344, 381, 529, 600, and 645 nm. Notably, the PBG at 600 nm showed the greatest spectral overlap with the PL emission of the CaZnOS:Mn phosphor layer, yielding the highest g_{PL} value of −0.512 in this system. In contrast, the PL_591||CNC_344 combination, in which the PBG is spectrally distant from the 591 nm emission, exhibited a relatively smaller g_{PL} value, confirming the role of PBG tuning in modulating circular polarization. Notably, five reproducible and independent measurements were conducted, confirming that the PBG effect modulating the g_{PL} values is repeatable and reliable. Furthermore, CPL, g_{PL}, and DC spectra were recorded after rotating the PL_591||CNC_600 sample by 90° along the incident-light axis (Figure S8, Supporting Information). The negligible changes in the CPL, g_{PL}, and DC spectra confirm that the observed CPL is not a result of linear-polarization emission. To validate the generality of the CPML platform and the role of the PBG effect further, we extended the system to commercially available ZnS:Cu phosphors. As shown in Figure S9 (Supporting Information), the PBG centered at 529 nm shows the most significant spectral overlap with the photoluminescent emission of ZnS:Cu@PDMS; therefore, it is expected to yield optimized g_{PL} values. So, the PL_503||CNC_529 sample produced the highest g_{PL} value of −0.538 (Figure S10 and Table S2, Supporting Information), confirming the efficacy of PBG tuning in enhancing CPL dissymmetry. Although the above system showed desirable CPL performance, neither the phosphor layer nor its individual components displayed any intrinsic CPL activity or characteristics of chiral structures (Figures S11 and S12, Supporting Information). This further confirms that the observed CPL signals originated from the chiroptical structure of the CNCs. To date, the correlation between CPL properties and excitation-source intensity

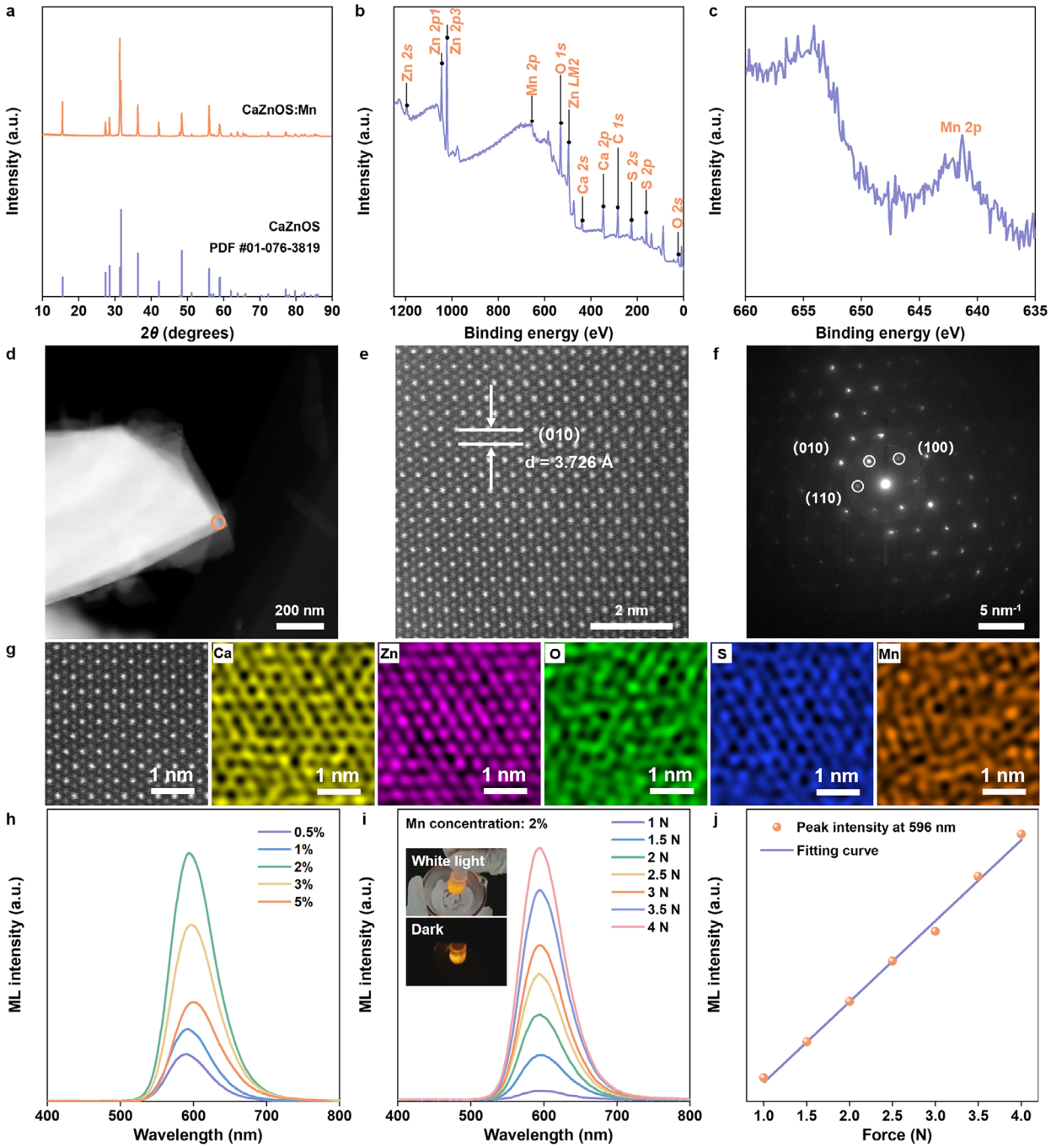

Figure 2. Characterization of CaZnOS:Mn phosphors. a) XRD pattern. b) Full-range and c) enlarged X-ray photoelectron spectroscopy measurements. d) High-angle annular dark-field scanning transmission electron microscopy image. e) High-resolution TEM image. f) Selected area electron diffraction image. g) High-resolution lattice image and corresponding energy dispersive spectroscopy maps of each element (Ca, Zn, O, S, and Mn). h) ML spectra with various Mn concentrations. i,j) ML spectra as a function of applied force for 2% Mn-doped samples. Inset: photographs of CaZnOS:Mn phosphors under white light and in the dark during mechanical excitation using a mortar and pestle.

has rarely been investigated. To address this issue, we examined the CPL response under varying excitation voltages. As shown in Figure S13 (Supporting Information), increasing the excitation voltage from 620 to 740 V resulted in pronounced changes in both the DC and CPL spectra. In contrast, the corresponding g_{PL} values showed negligible variation (Figure 3f; Figure S13 and Table S3, Supporting Information), indicating that the CPL asymmetry was largely unaffected by changes in the excitation intensity.

Owing to the distinctive ML properties of CaZnOS:Mn, we examined the circularly polarized characteristics of the ML emission from our proposed CPML platform. Although

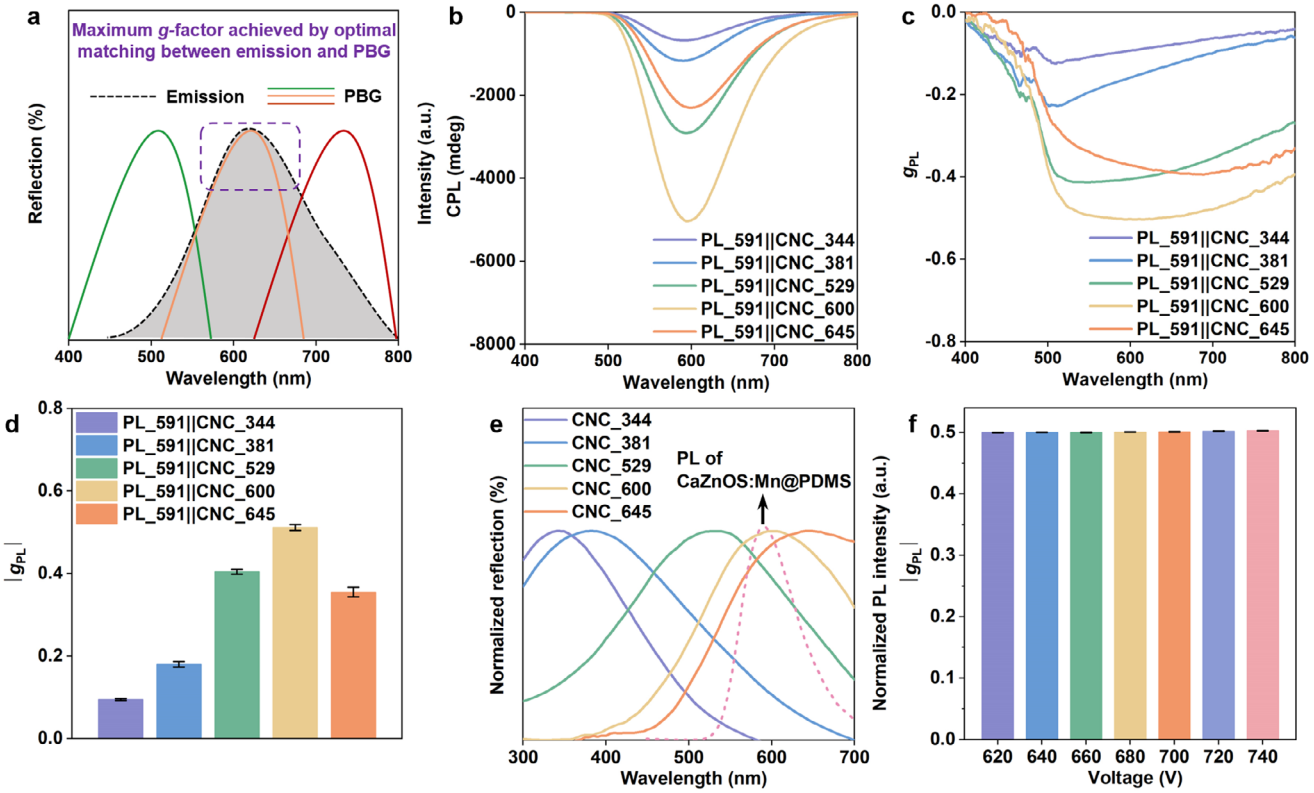

Figure 3. CPL properties with different PBGs (employing CaZnOS:Mn@PDMS as phosphor layer). a) g_{lum}-optimization mechanism via the PBG effect. b) CPL spectra. c) g_{PL} curves. d) g_{PL} values from five reproducible independent measurements ($n = 5$; mean ± standard deviation). e) Reflection spectra of CNC PC layers with different PBGs and PL spectrum of CaZnOS:Mn@PDMS. f) g_{PL} values of PL_591||CNC_600 under different excitation voltages ($n = 5$; mean ± standard deviation).

conventional CPL spectrometers are commonly used to quantify the luminescence asymmetry of chiral fluorophores, they may not be suitable for our system because a large linear motor cannot be accommodated within the spectrometer sample chamber. To overcome this limitation, we adapted a fiber-optic spectrometer to enable asymmetric measurements (**Figure 4a**). Specifically, a linear polarizer was positioned in front of the photodetector of the spectrometer, and the CPML sample was observed through a quarter-wave plate (converting L-CPL and R-CPL to linear-polarized light with a plane of polarization at ± 45° relative to the fast axis of the optic). As shown in Figure 4b, the handedness of the CPML emission was first evaluated through azimuthal angle-dependent intensity measurements, revealing a characteristic hourglass profile. The maximum and minimum intensities are observed at −45°/135° and 45°/225°, respectively. This polarization behavior is consistent with that of the right-handed emissions. Furthermore, the quarter-wave plate was removed, and the azimuthal-transmission profile was re-examined (Figure S14, Supporting Information). These results clearly demonstrate that mechano-induced CPL arises from chirality transmission and the mode dependence of photons during resonance in inhomogeneous helical microstructures.

The g_{ML} values were calculated using $g_{ML} = 2(I_L - I_R)/(I_L + I_R)$, where I_L and I_R represent the intensities of L-CPML and R-CPML, respectively. To obtain these values, we collected opposite-handed CPML intensities (Figure S15, Supporting Information) using a lab-made measurement system and applied the above equation for quantitative analysis. As shown in Figure 4c and Table S4 (Supporting Information), the measured g_{ML} values are −0.089, −0.163, −0.426, −0.573, and −0.342. Among these, the ML_596||CNC_600 sample exhibits the highest g_{ML} value of −0.573, which corresponds to the optimal spectral overlap between the 596-nm ML emission and 600-nm PBG (Figure 4d). In contrast, when the ML emission shifted away from the 600-nm PBG, the corresponding g_{ML} values gradually decreased.

Next, the system was extended to commercially available ZnS:Cu phosphors to demonstrate the general applicability of the PBG effect on ML. As shown in Figure S16 and Table S5 (Supporting Information), the ML_519||CNC_529 sample has the highest g_{ML} value of −0.540, attributed to the strong spectral overlap between the ML emission of ZnS:Cu and PBG centers at 529 nm (Figure S9, Supporting Information). These consistent and reproducible results highlight the pivotal role of PBG tuning in modulating the circular polarization of the ML emissions.

Further, the durability of the CPML platform was evaluated by continuous mechanical cycling. As shown in Figure 4e and Figure S17 (Supporting Information), the CPML emission and g_{ML} values of the ML_596||CNC_600 sample were monitored over 2000 sliding cycles in continuous scratching mode. Its excellent flexibility, recoverability, and stability render it well-suited for diverse applications, such as mechanical sensing and wearable electronics. As previously discussed, the emission intensity of

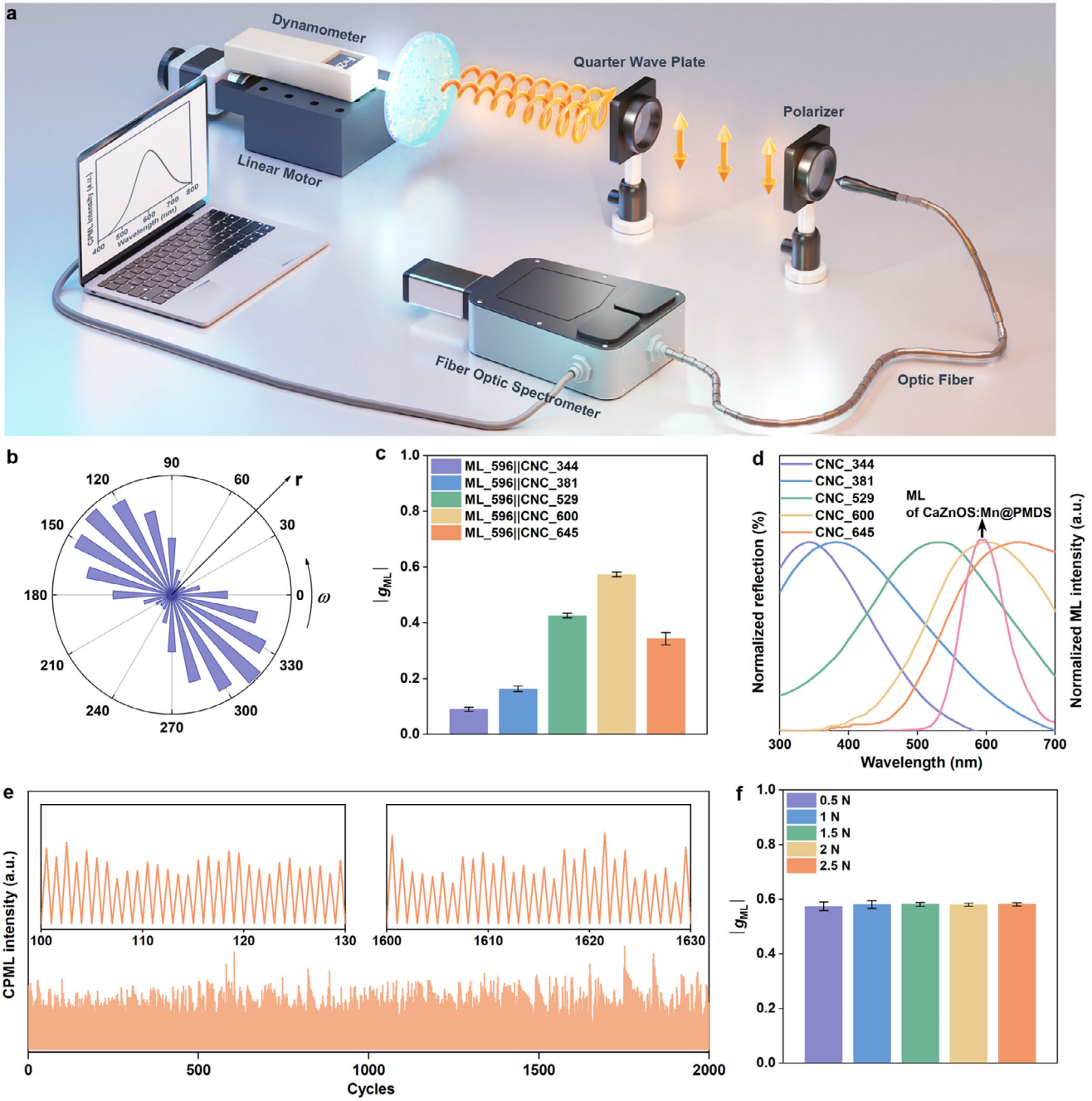

Figure 4. CPML properties with different PBGs (employing CaZnOS:Mn@PDMS as the phosphor layer). a) Schematic of g_{ML} measurements using a fiber-optic spectrometer equipped with a quarter-wave plate and linear polarizer. b) CPML intensity after passing through a quarter-wave plate and polarizer. c) g_{ML} values of CPML platform with different PBGs from five reproducible independent measurements ($n = 5$; mean ± standard deviation). d) Normalized reflection spectra of CNC PC layers with different PBGs, as well as the ML spectrum of CaZnOS:Mn@PDMS. e) Stability and repeatability tests of as-obtained ML_596||CNC_600 over 2000 cycles, with an inset providing a detailed view of the test over 100 cycles. f) g_{ML} values of ML_596||CNC_600 under different applied forces ($n = 5$; mean ± standard deviation).

ML materials increases with the applied force, whereas the CPL asymmetry remains largely independent of the excitation intensity. To examine the force dependence of the CPML further, we investigated the relationship between the applied force and the corresponding CPML dissymmetry factor. As shown in Figure 4f and Figure S18 and Table S6 (Supporting Information), increasing the applied force from 0.5 to 2.5 N results in a negligible variation in the g_{ML} value, confirming that the CPML asymmetry is effectively insensitive to changes in mechanical stimulus.

Theoretically, any stimulus capable of altering the P value of chiral nematic CNCs can modulate the PBG. In addition to the additive-agent concentration, stimuli such as water or

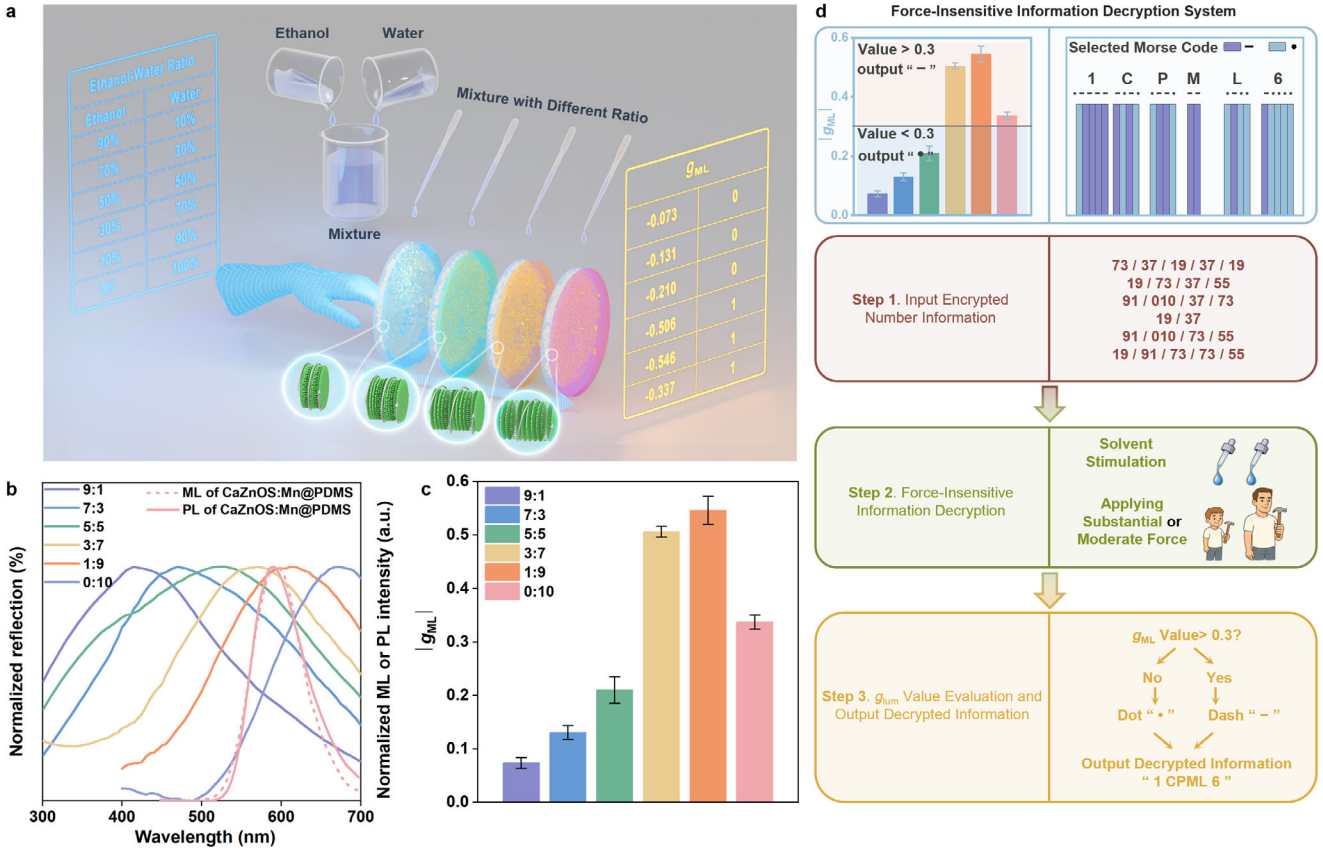

Figure 5. Solvent-responsive characteristics of the as-prepared CPML platform. a) Schematic of the solvent-responsive g_{ML}. b) Normalized reflection spectra of PC layers stimulated by ethanol-water mixtures, as well as the ML (and PL) spectra of CaZnOS:Mn@PDMS. c) g_{ML} values of the ML_596||CNC_600 sample when exposed to ethanol-water mixtures with different volume ratios ($n = 5$; mean ± standard deviation). d) Force-insensitive optical-decryption process demonstrating the encoded information "1CPML6.".

humidity can also influence *P*. We examined the effect of ethanol-water mixtures on the g_{ML} values. **Figure 5a** shows the solvent-responsive CPML behavior of the platform; when the PC layer is exposed to the solvent mixture and a mechanical force is simultaneously applied to the phosphor layer, a stable g_{ML} signal is achieved. Upon stimulation with the solvent mixture, the PC layer undergoes structural changes that shift the PBG (Figure 5b). As the water content in the ethanol-water mixture increases, the reflection band of the PC layer is progressively redshifted. Notably, when the ethanol-water ratio reached 1:9, the PBG shifted to 612 nm, closely matching the ML emission of the CaZnOS:Mn@PDMS layer. This spectral alignment results in the highest measured g_{ML} value (−0.546) for the ML_596||CNC_600 sample based on the PBG effect (Figure 5c; Figure S19 and Table S7, Supporting Information). This exploration establishes a new mode of signal transduction, wherein the composition of the solvent-mixture ratio is directly translated into distinct g_{ML} outputs under mechanical force. The strong correspondence and force-insensitivity properties between the solvent-mixture ratio and g_{ML}-value output enable precise information readout without signal overlap or susceptibility to environmental perturbations. A representative demonstration of force-insensitive optical decryption is shown in Figure 5d, where Morse code was utilized as the information carrier. Dashes ("-") and dots ("•") were selected to encode information through combinatorial arrangements representing alphanumeric characters. The decryption process began by applying a mechanical force at a predefined solvent ratio, which served as an encryption key inaccessible to unauthorized users. The resulting g_{ML} value was used as the decoding criterion. Specifically, a g_{ML}-value threshold of 0.3 was employed, values above 0.3 were interpreted as "-" and those below 0.3 as "•." Using this binary optical readout, "1CPML6" was successfully decoded. This Morse-code-based decryption protocol, coupled with CPML, ensures high decoding fidelity while guaranteeing that valid decryption is accessible only to authorized individuals.

3. Conclusion

In conclusion, we developed a CPML platform by integrating a ML phosphor layer with a PC layer. This platform represents a notable advancement in the design of innovative and reusable chiral luminescent materials, achieving effective chirality control while eliminating dependence on photoexcitation. By precisely tuning the chiral nematic structure of the PC layer through modulation with glucose, we achieved adjustable PBGs, obtaining a maximum g_{PL} of −0.512 and g_{ML} of −0.573. In addition to the PBG-governed chiroptical performance, the resulting platform

exhibited a distinct solvent-responsive CPML behavior, enabling the effective detection and sensing of ethanol-water mixture ratios. Due to the force-insensitive nature of the chiral signal, this platform offers a new strategy for information decryption that can operate under light-free or autonomous conditions, ensuring both the accuracy and security of the information while simplifying the decryption process. Our findings advance the understanding of CPML systems mediated by photonic band structures and underscore the potential of this CPML platform in future applications involving chiroptical sensing and secure information technologies.

Supporting Information

Supporting Information is available from the Wiley Online Library or from the author.

Acknowledgements

This work was supported by the National Natural Science Foundation of China (52372154, U22A2077, 12074263, and 62275170), the Guangdong Basic and Applied Basic Research Foundation (2025A1515012171, 2023A1515110267), the Guangdong Provincial Science Fund for Distinguished Young Scholars (2022B1515020054), the Shenzhen Science and Technology Innovation Commission (JCYJ20240813142628038), and the Shenzhen High-End Talent Scientific Research Program, and the Scientific Foundation for Youth Scholars of Shenzhen University. The authors also acknowledge the Electron Microscopy Center of Shenzhen University for performing the high-resolution TEM observation.

Conflict of Interest

The authors declare no conflict of interest.

Author Contributions

X.N., C.W., D.Z., and C.P. conceived the idea for this work. X.N. prepared the samples, conducted the experiments, collected, and analyzed the data. X.N., C.W., D.Z., and C.P. wrote and revised the manuscript. X.L., G.L., Z.L., and D.P. conducted the formal analysis.

Data Availability Statement

The data that support the findings of this study are available from the corresponding author upon reasonable request.

Keywords

circularly polarized luminescence, information security, mechanoluminescence, smart sensors, stimuli-responsive materials

Received: October 8, 2025
Revised: November 13, 2025
Published online:

[1] M. Kim, M. Zhang, Y. L. Zhu, Y. Yan, X. Pu, W. Choi, S. Chung, K. Cho, J. Kim, V. Tsukruk, Z. Yang, N. A. Kotov, Z. Y. Lu, D. H. Kim, Z. Lin, *Science* **2025**, *389*, adu0296.
[2] R. Chowdhury, M. D. Preuss, H. H. Cho, J. J. P. Thompson, S. Sen, T. K. Baikie, P. Ghosh, Y. Boeije, X. W. Chua, K. W. Chang, E. Guo, J. van der Tol, B. W. L. van den Bersselaar, A. Taddeucci, N. Daub, D. M. Dekker, S. T. Keene, G. Vantomme, B. Ehrler, S. C. J. Meskers, A. Rao, B. Monserrat, E. W. Meijer, R. H. Friend, *Science* **2025**, *387*, 1175.
[3] A. P. M. Reponen, M. Mattes, Z. A. VanOrman, L. Estaque, G. Pieters, S. Feldmann, *Nature* **2025**, *643*, 675.
[4] A. Das, S. Ghosh, S. J. George, *Angew. Chem.* **2023**, *62*, 202308281.
[5] M. Xu, Z. Xu, M. A. Soto, Y. T. Xu, W. Y. Hamad, M. J. MacLachlan, *Adv. Mater.* **2023**, *25*, 2301060.
[6] M. M. Zhang, R. Zhang, S. Y. Yang, X. Y. Dong, C. Zhang, Y. Si, T. Jia, Z. Han, S. Q. Zang, T. C. W. Mak, *Adv. Mater.* **2025**, *37*, 2502899.
[7] C. Shi, J. M. Jin, R. J. Wang, W. C. Chen, C. L. Sun, S. Ji, Y. Huo, H. L. Zhang, *Adv. Mater.* **2025**, *37*, 2420611.
[8] S. Wang, S. Wu, R. Wang, J. Lu, M. Liu, *Angew. Chem.* **2025**, *64*, 202507992.
[9] H. Li, X. Zhang, C. Tan, P. Zhang, F. Zhao, S. Guo, Y. Qi, H. Li, G. Xie, Y. Tao, R. Chen, W. Huang, *Adv. Mater.* **2025**, *37*, 2500841.
[10] Q. Guo, Z. Li, Y. Zhou, S. Zhao, Y. Wang, M. Zhang, G. Li, Z. Tong, T. Zhuang, S. H. Yu, *Sci. Adv.* **2025**, *11*, adv2721.
[11] A. Ying, L. Zhan, Y. Tan, X. Cao, C. Yang, S. Gong, *Sci. China Chem.* **2023**, *66*, 2274.
[12] O. G. Willis, F. Zinna, L. Di Bari, *Angew. Chem.* **2023**, *62*, 202302358.
[13] X. Niu, Z. Zeng, Z. Wang, H. Lu, B. Sun, H. Zhang, Y. Chen, Y. Du, G. Long, *Sci. China Chem.* **2024**, *67*, 1961.
[14] T. Song, C. Q. Wang, H. Lu, X. J. Mu, B. L. Wang, J. Z. Liu, B. Ma, J. Cao, C. X. Sheng, G. Long, *Angew. Chem.* **2024**, *63*, 202400769.
[15] H. Liu, A. S. Portniagin, B. Tang, K. Vighnesh, Y. Li, Y. Wu, D. A. Rusanov, L. Ke, Y. Wang, D. Zhu, D. Chen, K. C. Law, M. V. Babak, E. Ushakova, A. L. Rogach, *ACS Nano* **2025**, *19*, 17774.
[16] Z. He, B. Sun, H. Lu, X. Sun, Z. Xu, Y. Liang, Q. Lu, Y. Yu, K. Hu, S. Poddar, W. Wu, W. Gao, X. Han, Z. Fan, C. Pan, *Sci. Adv.* **2025**, *11*, adw7826.
[17] G. Long, R. Sabatini, M. I. Saidaminov, G. Lakhwani, A. Rasmita, X. Liu, E. H. Sargent, W. Gao, *Nat. Rev. Mater.* **2020**, *5*, 423.
[18] Z. P. Yan, L. Yuan, Y. Zhang, M. X. Mao, X. J. Liao, H. X. Ni, Z. H. Wang, Z. An, Y. X. Zheng, J. L. Zuo, *Adv. Mater.* **2022**, *34*, 2204253.
[19] X. Yao, Z. Lin, X. Liu, H. Ma, X. Wang, W. Huang, Z. An, *Angew. Chem.* **2025**, *64*, 202510153.
[20] P. García-Cerezo, M. D. Codesal, A. H. G. David, L. L.e Bras, S. Abid, X. Li, D. Miguel, M. Kazem-Rostami, B. Champagne, A. G. Campaña, J. F. Stoddart, V. Blanco, *Adv. Mater.* **2025**, *37*, 2417326.
[21] M.-J. Ji, W.-L. Zhao, M. Li, C.-F. Chen, *Nat. Commun.* **2025**, *16*, 2940.
[22] B. Yuan, J. Qin, L. He, Z. Zhang, Y. Feng, L. Lv, X. Wang, C. Zou, M. Yu, Y. Chen, Y. Gao, H. Yang, *Adv. Funct. Mater.* **2025**, *35*, 2424601.
[23] J. Liu, X. Y. Zhou, J. Wei, J. J. Wu, J. X. Hu, X. Y. Fang, R. C. Lan, Y. Tao, Y. Ma, B. X. Li, H. Yang, Y. Q. Lu, Q. Zhao, *Adv. Funct. Mater.* **2025**, *35*, 2506911.
[24] G. Wu, X. Li, R. Bao, C. Pan, *Adv. Funct. Mater.* **2024**, *34*, 2405722.
[25] D. Lu, M. Li, X. Gao, X. Yu, L. Wei, S. Zhu, Y. Xu, *ACS Nano* **2022**, *17*, 461.
[26] W. Fan, J. Li, L. Wei, Y. Xu, *Carbohydr. Polym.* **2022**, *289*, 119442.
[27] J. Li, W. Qin, C. Li, Y. Yang, K. Liao, F. Yuan, *Adv. Funct. Mater.* **2025**, *35*, 2510409.
[28] M. Zhang, Q. Guo, Z. Li, Y. Zhou, S. Zhao, Z. Tong, Y. Wang, G. Li, S. Jin, M. Zhu, *Sci. Adv.* **2023**, *9*, adi9944.
[29] X. Nie, Y. Zhang, B. Wu, Z. Ye, F. Gao, Y. Chen, C. Wang, D. Zhu, P. Alam, Z. Qiu, B. Z. Tang, *ACS Nano* **2025**, *19*, 11221.
[30] X. Nie, S. Wu, P. Lv, H. Ke, F. Huang, Q. Wei, *Chem. Eng. J.* **2022**, *433*, 134410.
[31] J. He, R. Wei, S. Ge, W. Wu, J. Guo, J. Tao, R. Wang, C. Wang, C. Pan, *InfoMat* **2024**, *6*, 12493.
[32] C. Wang, H. Hu, D. Zhu, C. Pan, *Sci. Bull.* **2023**, *68*, 559.
[33] Y. Zhuang, R. J. Xie, *Adv. Mater.* **2021**, *33*, 2005925.

[34] S. Fang, L. Zhao, X. He, B. Zhou, Y. He, Z. Lu, Z. Wang, *Adv. Mater.* **2025**, *37*, 2505071.
[35] W. Li, S. Wu, J. Ren, P. Xiong, *Adv. Funct. Mater.* **2025**, *35*, 2506198.
[36] D. Peng, H. Li, J. Sun, Y. Deng, F. Jiao, Y. Han, K. Zhang, J. Meng, X. Li, L. Wang, L. M. Fu, Q. Hua, C. X. Shan, L. Dong, *Adv. Mater.* **2025**, *37*, 2503376.
[37] S. Liu, Y. Guo, Z. Song, D. Peng, Q. Liu, F. Wang, *Adv. Mater.* **2025**, *37*, 06957.
[38] J. Guo, F. Guo, H. Zhao, H. Yang, X. Du, F. Fan, W. Liu, Y. Zhang, D. Tu, J. Hao, *Adv. Mater.* **2025**, *37*, 2419405.
[39] X. Pan, Y. Zhuang, W. He, C. Lin, L. Mei, C. Chen, H. Xue, Z. Sun, C. Wang, D. Peng, Y. Zheng, C. Pan, L. Wang, R. J. Xie, *Nat. Commun.* **2024**, *15*, 2673.
[40] C. Chen, S. Zhao, C. Pan, Y. Zi, F. Wang, C. Yang, Z. L. Wang, *Nat. Commun.* **2022**, *13*, 1391.
[41] X. G. Zheng, I. Yamauchi, T. Galica, E. Nishibori, T. Kawae, J. G. Nakamura, A. Koda, C. N. Xu, *Adv. Sci.* **2025**, *12*, 09474.
[42] Y. Xi, P. Tan, Z. Li, Y. Fan, *Soft Sci.* **2023**, *3*, 26.
[43] Y. Lu, L. Ma, H. Zhang, Y. Mei, Z. Xiong, E. Song, *Soft Sci.* **2024**, *4*, 36.
[44] B. Hou, L. Yi, C. Li, H. Zhao, R. Zhang, B. Zhou, X. Liu, *Nat. Electron.* **2022**, *5*, 682.
[45] W. Yang, H. Liu, H. Du, M. Zhang, C. Wang, R. Yin, C. Pan, C. Liu, C. Shen, *Sci. China Mater.* **2023**, *66*, 2829.
[46] Z. Xu, X. Han, W. Wu, F. Li, R. Wang, H. Lu, Q. Lu, B. Ge, N. Cheng, X. Li, G. Yao, H. Hong, K. Liu, C. Pan, *Light: Sci. Appl.* **2023**, *12*, 67.
[47] Y. Zhang, Q. Lu, J. He, Z. Huo, R. Zhou, X. Han, M. Jia, C. Pan, Z. L. Wang, J. Zhai, *Nat. Commun.* **2023**, *14*, 1252.
[48] M. Qi, R. Yang, Z. Wang, Y. Liu, Q. Zhang, B. He, K. Li, Q. Yang, L. Wei, C. Pan, M. Chen, *Adv. Funct. Mater.* **2023**, *33*, 2214479.
[49] X. Sun, S. Ling, Z. Qin, J. Zhou, Q. Shi, Z. Liu, Y. J. Tan, *Adv. Mater.* **2025**, *37*, 2502743.
[50] Y. Zhao, R. Wu, Y. Hao, Y. Zhao, X. Zhang, H. Liu, W. Zhai, K, D., C. Pan, C. Liu, C. Shen, *Adv. Mater.* **2025**, *37*, 2507127.
[51] Z. Yang, S. Huo, Z. Zhang, F. Meng, B. Liu, Y. Wang, X. Ma, Z. Wang, J. Xu, Q. Tian, Y. Wang, Y. Ding, X. Hu, Y. Xie, S. Fan, C. Pan, E. Wu, *Adv. Funct. Mater.* **2025**, *35*, 2509119.
[52] X. Han, J. Tao, Y. Liang, F. Guo, Z. Xu, W. Wu, J. Tong, M. Chen, C. Pan, J. Hao, *Nat. Commun.* **2024**, *15*, 10430.
[53] Y. Liu, J. Tao, Y. Mo, R. Bao, C. Pan, *Adv. Mater.* **2024**, *36*, 2313857.
[54] X. He, Y. Zheng, Z. Luo, Y. Wei, Y. Liu, C. Xie, C. Li, D. Peng, Z. Quan, *Adv. Mater.* **2024**, *36*, 2309906.
[55] Y. Liu, Y. Wei, Z. Quan, *Acc. Mater. Res.* **2025**, *6*, 638.
[56] C. Wang, H. Hu, D. Peng, L. Dong, D. Zhu, *Soft Sci.* **2023**, *3*, 39.